Heat Transfer of Buoyancy and Radiation on the Free Convection Boundary Layer MHD Flow across a Stretchable Porous Sheet

Hari M. Srivastava, Ziad Khan, Pshtiwan Othman Mohammed, Eman Al-Sarairah, Muhammad Jawad, and Rashid Jan

2022

energies

MDPI

Article

Heat Transfer of Buoyancy and Radiation on the Free Convection Boundary Layer MHD Flow across a Stretchable Porous Sheet

Hari Mohan Srivastava [1,2,3,4,*], Ziad Khan [5], Pshtiwan Othman Mohammed [6], Eman Al-Sarairah [7,8], Muhammad Jawad [5] and Rashid Jan [5]

1 Department of Mathematics and Statistics, University of Victoria, Victoria, BC V8W 3R4, Canada
2 Department of Medical Research, China Medical University Hospital, China Medical University, Taichung 40402, Taiwan
3 Department of Mathematics and Informatics, Azerbaijan University, 71 Jeyhun Hajibeyli Street, AZ1007 Baku, Azerbaijan
4 Center for Converging Humanities, Kyung Hee University, 26 Kyungheedae-ro, Dongdaemun-gu, Seoul 02447, Republic of Korea
5 Department of Mathematics, University of Swabi, Swabi 23561, KPK, Pakistan
6 Department of Mathematics, College of Education, University of Sulaimani, Sulaimani 46001, Iraq
7 Department of Mathematics, Khalifa University, Abu Dhabi P.O. Box 127788, United Arab Emirates
8 Department of Mathematics, Al-Hussein Bin Talal University, Ma'an P.O. Box 33011, Jordan
* Correspondence: harimsri@math.uvic.ca

Abstract: Theoretical influence of the buoyancy and thermal radiation effects on the MHD (magnetohydrodynamics) flow across a stretchable porous sheet were analyzed in the present study. The Darcy–Forchheimer model and laminar flow were considered for the flow problem that was investigated. The flow was taken to incorporate a temperature-dependent heat source or sink. The study also incorporated the influences of Brownian motion and thermophoresis. The general form of the buoyancy term in the momentum equation for a free convection boundary layer is derived in this study. A favorable comparison with earlier published studies was achieved. Graphs were used to investigate and explain how different physical parameters affect the velocity, the temperature, and the concentration field. Additionally, tables are included in order to discuss the outcomes of the Sherwood number, the Nusselt number, and skin friction. The fundamental governing partial differential equations (PDEs), which are used in the modeling and analysis of the MHD flow problem, were transformed into a collection of ordinary differential equations (ODEs) by utilizing the similarity transformation. A semi-analytical approach homotopy analysis method (HAM) was applied for approximating the solutions of the modeled equations. The model finds several important applications, such as steel rolling, nuclear explosions, cooling of transmission lines, heating of the room by the use of a radiator, cooling the reactor core in nuclear power plants, design of fins, solar power technology, combustion chambers, astrophysical flow, electric transformers, and rectifiers. Among the various outcomes of the study, it was discovered that skin friction surges for $0.3 \leq F_1 \leq 0.6$, $0.1 \leq k_1 \leq 0.4$ and $0.3 \leq M \leq 1.0$, snf declines for $1.0 \leq G_r \leq 4.0$. Moreover, the Nusselt number augments for $0.5 \leq R \leq 1.5$, $0.2 \leq N_t \leq 0.8$ and $0.3 \leq N_b \leq 0.9$, and declines for $2.5 \leq Pr \leq 5.5$. The Sherwood number increases for $0.2 \leq N_t \leq 0.8$ and $0.3 \leq Sc \leq 0.9$, and decreases for $0.1 \leq N_b \leq 0.7$.

Keywords: heat transfer; MHD (magnetohydrodynamics) flow; stretching porous sheet; free convection

MSC: 26A51; 26A33; 26D10

Citation: Srivastava, H.M.; Khan, Z.; Mohammed, P.O.; Al-Sarairah, E.; Jawad, M.; Jan, R. Heat Transfer of Buoyancy and Radiation on the Free Convection Boundary Layer MHD Flow across a Stretchable Porous Sheet. *Energies* **2023**, *16*, 58. https://doi.org/10.3390/en16010058

Academic Editor: Ziemowit Malecha

Received: 17 November 2022
Revised: 10 December 2022
Accepted: 16 December 2022
Published: 21 December 2022

1. Introduction and Motivation

Magnetohydrodynamics (MHD) is the study of the magnetic impact of an electrically conducted incompressible fluid; it has received attention because of its major applications

in different areas, such as X-ray radiation, crystal growth, asthma treatment, tumor therapy, plasma, fusing metal in electric heaters, nuclear reactors, gastric medication, and electrolytic biomedicine. MHD fluid can also be used to manage the cooling rates in certain industrial processes. With homogeneous magnetic fields, Chaudhary and Kumar [1] explored an unsteady 2D flow of an electrically conducted fluid toward a stretchable sheet. Naramgari and Sulochana [2] analyzed the chemical reaction and thermal radiation effects on a two-dimensional MHD steady flow toward a stretchable sheet using injection/suction. By using a chemical reaction, Reddy et al. [3] analyzed the impacts of MHD and buoyancy forces through rotating vertically porous plates. Mishra and Jena [4] explored steady two-dimensional incompressible, laminar, and electrically conducted fluids toward a stretchable sheet using magnetic fields and the viscous dissipation effect. Babu et al. [5] found numerical solutions of a steady two-dimensional MHD boundary layer flow toward a shrinking sheet by using the wall mass suction effect. Using the homotopy analysis method (HAM) technique, Mabood et al. [6] found the impact of radiation on the MHD flow toward an exponential stretchable sheet. Pal and Mondal [7] investigated heat transfer characteristics and the MHD non-Darcy boundary layer flow toward an electrically conducted fluid in the presence of the viscosity impact. The researchers in [8] demonstrated the MHD natural convection-based nanofluid flow toward a porous surface. Using the radiation effect, Mahmoud [9] investigated the heat transport flow of electrically conducted fluids across continuously moving vertical infinite plates with heat flux and suction. With variable heat, radiation effect, and mass diffusion, Kishore et al. [10] described the viscous incompressible MHD flow in porous media. Majeed et al. [11] evaluated the impact of energy activation and chemical reactions on the two-dimensional flow of heat transfer toward an exponential stretchable surface. With radiation influence and the boundary layer flow of viscous fluid, Sharma et al. [12] solved the problem of heat transfer due to an exponentially stretching/shrinking sheet. Poornima and Reddy [13] found the mathematical solutions of the convective flow of radiating boundary layer-combined nanofluids to a non-linear movable sheet using induced magnetic fields. Some studies involving MHD flow and thermal radiation have also been published in [14–20]. The researchers in [21] discussed the heat generation and Cattaneo–Christov heat flux effect on a hybrid nanofluid flow over two distinct geometries. Yaseen et al. [22] explored the Darcy–Forchheimer model and Cattaneo–Christov heat flux of MoS_2-SiO_2/kerosene oil between shrinking and rotating disks. Khan et al. [23] investigated the magnetohydrodynamic thin film flow through a porous stretching sheet by focusing on the impact of thermal radiation and viscous dissipation. Jawad et al. [24] discussed the analysis of the hybrid nanofluid stagnation point flow over a stretching surface by focusing on melting heat transfer.

Heat transfer analysis toward a porous stretchable sheet has received a lot of attention from architects, geologists, engineers, and mathematicians due to its occurrence in many practical and scientific situations, such as electronic cooling, thermal insulation, catalytic reactor, nuclear waste repository, oil production, geothermal system, petroleum industries, and energy storage units (see [25–28]). In 1856, Henry Darcy worked with homogeneous fluid flow passing through a porous medium. However, the classical Darcy law did not work for higher permeability flows and large velocities. In order to overcome this demerit, the researchers in [29] revised the Darcy velocity formula by including the velocity square into the equation of momentum to calculate the boundary layer flow and inertial effects. Pal and Mondal [30] described the Darcy–Forchheimer model to examine the mixed convection flow of a stretchable sheet using thermal radiation and variable viscosity. Ganesh et al. [31] examined the Darcy–Forchheimer model and hydromagnetic nanofluids on stretchable surfaces. The Darcy–Forchheimer–Casson fluid flow was investigated by Seth and Mandal [32], who discovered the influences of rotational and Casson parameters on the primary velocity. Under the saturated porous medium of the Darcy–Forchheimer flow, Seddeek [33] investigated the combined effects of viscous dissipation and the thermophoresis parameter. Hayat et al. [34] evaluated the 2D Darcy–Forchheimer flow of Maxwell fluids, induced by a stretchable sheet. Rajesh et al. [35] examined the heat transfer

rate and the hybrid nanoparticle impact on the MHD flow through a vertical plate. The researchers in [36] studied the heat transfer analysis of nanoparticles (MoS_2/H_2O) and hybrid nanoparticles (MoS_2-SiO_2/H_2O-$C_2H_6O_2$) between two distinct plates by using heat absorption/generation. Raza et al. [37] explored the influence of Joules heating and the Brownian motion radiative nanofluid toward a stretchable cylinder. Faizan et al. [38] described the behaviors of heat and mass transfer for the Cattaneo–Christov nanofluid toward a Riga sheet.

The injection and suction have remarkable effects on boundary layer flow surfaces. The suction is used to upsurge the skin friction, whereas the injection works in the opposite direction. The injection of fluids through a porous sheet has practical applications in the boundary layer problem, such as wire coating, polymer fiber coating, and film cooling. Furthermore, they are important in the field of engineering, e.g., regarding radial diffusion and the construction of thrust bearings (see [39]). Suction is utilized in chemical progression to remove the reactant, whereas blowing is used to introduce a reactant, cool the surfaces, minimize the drag, and prevent corrosion (see [40–42]).

Many phenomena in applied sciences and engineering fields are governed by non-linear BVPs. As a result, BVPs have received attention from engineers, mathematicians, and physicists. Generally speaking, compared to linear ODEs and PDEs, it is significantly more complicated to find the analytical solutions of non-linear ODEs and PDEs, particularly when using analytical methods. Therefore, in 1992, Liao [43] proposed the homotopy analysis method (HAM) [44–48], relying on homotopy in topology. This approach is unaffected by significant large/small physical variations. The HAM approach provides great versatility in terms of changing and choosing the convergence areas and estimating rates. The method has an advantage over typical computational methodologies in that it avoids rounding off errors induced by the discretization procedure.

Judging by the aforementioned and other related literature studies, numerous studies have been presented for buoyancy and radiation influence on the MHD flow toward a stretchable sheet; however, limited studies are available for the Darcy–Forchheimer model with the Brownian motion, heat source, sink, or the thermophoresis effect on the MHD flow across a stretchable porous sheet. Therefore, the present study fills this gap. The novelty of this study is that it enhances the work of Daniel [49] by introducing the species conservation equation and the Darcy–Forchheimer model with the influence of the Brownian motion, heat source, heat sink, or thermophoresis effect on the MHD flow across a stretchable porous sheet. The general form of the buoyancy term in the momentum equation for a free convection boundary layer is derived in this study. The fluid flow is considered laminar, incompressible, and electrically conducted. *Mathematica* software and homotopy analysis techniques were utilized to solve the modeled equations. The variations of several physical parameters on the flow, as well as thermal and concentration characteristics, are discussed briefly. The present study provides several applications, such as film cooling, wire coating, polymer fiber coating, construction of thrust bearings, radial diffusion, oil production, thermal insulation, X-ray radiation, fusing metal in electric heaters, and gastric medication.

The present study provides the following research questions:

1. What is the general form of the buoyancy term in the momentum equation for a free convection boundary layer? How may it be approximated if the flow is due to temperature variations? What is the name of the approximation?
2. What physical processes are represented by the terms of the momentum Equation (19)? By the energy Equation (20)? By the species conservation Equation (21)?
3. What is the definition of the Prandtl number? How does its value affect the relative growth of the thermal boundary layer for the laminar flow toward a porous stretching sheet?

2. Preliminaries

It is commonly recognized that non-linear PDEs and ODEs for BVPs are significantly harder to solve than linear PDEs and ODEs, particularly when we attempt to use analytical

techniques. Traditionally, asymptotic and perturbation approaches are frequently used to obtain analytic approximations of non-linear problems in engineering. Unfortunately, asymptotic and perturbation methods only work for weak nonlinear systems because they generally rely too heavily on small/large physical parameters. Therefore, certain analytical approximation techniques must be developed to be applicable to extremely non-linear problems, independently of any large/small physical parameters. Thus, in 1992, Liao [43] developed one of these semi-analytic approximation techniques.

We begin by presenting the following nonlinear differential equation:

$$\mathcal{N}_1[u_1(x_1,t_1)] = 0, \tag{1}$$

where $\mathcal{N}_1$ and $u_1(x_1,t_1)$ represent the nonlinear operator and the unknown function, respectively. Liao [43] introduced a two-parameter set of equations in the embedded parameter $p \in [0,1]$, which is known as the 0th-order deformation equation given by

$$(1-p)\mathcal{L}_1[\phi(x_1,t_1;p) - u_0(x_1,t_1)] = \hbar p \mathcal{N}_1[\phi(x_1,t_1;p)], \tag{2}$$

where $\mathcal{L}_1$, $\phi(x_1,t_1;p)$ and $u_0(x_1)$ represent an auxiliary linear-operator, unknown function, and initial guess, respectively. We find at $p = 0$ and $p = 1$ that

$$\phi(x_1,t_1;0) = u_0(x_1,t_1), \tag{3}$$

and

$$\phi(x_1,t_1;1) = u_1(x_1,t_1). \tag{4}$$

The solution $\phi(x_1,t_1;p)$ of the 0th-order deformation equation distorts from the initial estimate $u_0(x_1,t_1)$ to the actual solution $u_1(x_1,t_1)$ of the given equation $\mathcal{N}_1[u_1(x_1,t_1)] = 0$ as the embedded parameter $p \in [0,1]$ increases from 0 to 1. We can extend $\phi(x_1,t_1;p)$ into a Maclaurin expansion with respect to p because it also depends on the embedded parameter $p \in [0,1]$, as follows:

$$\phi(x_1,t_1;p) = u_0(x_1,t_1) + \sum_{m=1}^{\infty} u_m(x_1,t_1)p^m, \tag{5}$$

where

$$u_m(x_1,t_1) = \frac{1}{m!}\frac{\partial^m \phi(x_1,t_1;p)}{\partial p^m}\Big|_{p=0}. \tag{6}$$

Equation (5) is known as the homotopy Maclaurin expansion of $\phi(x_1,t_1;p)$. Particularly, at $p = 1$, we have

$$\phi(x_1,t_1;1) = u_0(x_1,t_1) + \sum_{m=1}^{\infty} u_m(x_1,t_1). \tag{7}$$

We obtain the following homotopy series solution if the aforementioned series converges to $\phi(x_1,t_1;1)$, as indicated by Equation (4):

$$u_1(x_1,t_1) = u_0(x_1,t_1) + \sum_{m=1}^{\infty} u_m(x_1,t_1), \tag{8}$$

which satisfies the given equation $\mathcal{N}_1[u_1(x_1,t_1)] = 0$ as proven by Liao [43]. Equation $u_m(x_1,t_1)$ is entirely determined by means of Equation (2). Taking the derivative of Equation (2) m times with respect to the embedded parameter p, if we divide by $m!$ and finally put $p = 0$, then we have

$$\mathcal{L}_1[u_m(x_1,t_1) - \chi_m u_{m-1}(x_1,t_1)] = \hbar \mathcal{D}_{m-1}\mathcal{N}_1[\phi(x_1,t_1;p)], \tag{9}$$

where

$$\mathscr{D}_{m-1} = \frac{1}{(m-1)!}\frac{\partial^{m-1}}{\partial p^{m-1}}\Big|_{p=0}, \tag{10}$$

and

$$\chi_m = \begin{cases} 0, & \text{if} \quad m \leq 1 \\ 1, & \text{if} \quad m > 1. \end{cases} \tag{11}$$

3. Mathematical Formulation

Here, we assume a steady, incompressible, and electrically conducted MHD flow toward a stretching porous sheet that is driven by the buoyancy forces. We also assume that the fluid flow is a laminar, two-dimensional, constant property condition in which the gravity force acts in the negative x-direction. A uniform magnetic field is applied normally to the sheet. The exception is for the influence of the variable density in the buoyancy force since it is this variation that induces fluid motion. The x-axis is taken along the stretching sheet in the direction of the motion while the y-axis is perpendicular to the sheet. Geometric representation of the physical flow model is shown in Figure 1. The transverse applied magnetic field and magnetic Reynolds number are assumed to be very small. Viscous dissipation, induced magnetic field, and the pressure gradient are considered negligible.

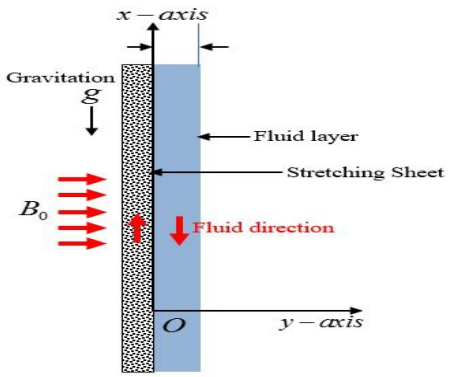

Figure 1. Geometry of the physical flow problem.

Under the above-stated assumption, the continuity equation is written as:

$$\frac{\partial u}{\partial x} + \frac{\partial v}{\partial y} = 0, \tag{12}$$

here, the term represents the net outflow (outflow minus inflow) of the mass in the x and y directions, the sum of which must be zero for the steady flow.

The appropriate form of the momentum equation can be represented as:

$$u\frac{\partial u}{\partial x} + v\frac{\partial u}{\partial y} = v\frac{\partial^2 u}{\partial y^2} - \frac{\sigma B_0^2(x)}{\rho}u - \frac{dp_\infty}{\rho dx} - g_1 - u\frac{v}{k_0} - F_0 u^2, \tag{13}$$

where $\frac{dp_\infty}{\rho dx}$ is the free stream pressure gradient in the region outside the boundary layer. In this region, u = 0, then we have

$$\frac{dp_\infty}{\rho dx} = -\rho_\infty g_1, \tag{14}$$

substituting Equation (14) into Equation (13), we obtain the following expression:

$$u\frac{\partial u}{\partial x} + v\frac{\partial u}{\partial y} = v\frac{\partial^2 u}{\partial y^2} - \frac{\sigma B_0^2(x)}{\rho}u + g_1(\Delta\rho/\rho) - u\frac{v}{k_0} - F_0 u^2, \tag{15}$$

where $\Delta\rho = \rho_\infty - \rho$.

The third component on the right side of Equation (15) is the buoyancy force; the fluid flow originates because the density ρ is a parameter. If the ρ variation is only due to the temperature variation, then the component may be linked to a fluid property known as the volumetric thermal expansion coefficient.

$$\beta_1 = -\frac{1}{\rho}\left(\frac{\partial \rho}{\partial T}\right)_p. \tag{16}$$

This thermodynamic property of the fluid provides a measure of the amount by which the density change responds to a change in the temperature at constant pressure. It is expressed in the following approximate form

$$\beta_1 \approx \frac{\Delta\rho}{\rho\Delta T} = -\frac{1}{\rho}\left(\frac{\rho_\infty - \rho}{T_\infty - T}\right), \tag{17}$$

it follows that

$$(\rho_\infty - \rho) \approx \rho\beta_1(T - T_\infty). \tag{18}$$

This simplification is known as the Boussinesq approximation, and substituting into Equation (15), we obtain the following constituted boundary layers governing the equation (see Daniel [49] and Chamkha [50]):

$$u\frac{\partial u}{\partial x} + v\frac{\partial u}{\partial y} = v\frac{\partial^2 u}{\partial y^2} - \frac{\sigma B_0^2(x)}{\rho}u + g_1\beta_1(T - T_\infty) - u\frac{v}{k_0} - F_0u^2, \tag{19}$$

$$u\frac{\partial T}{\partial x} + v\frac{\partial T}{\partial y} = \alpha\frac{\partial^2 T}{\partial y^2} + \frac{Q_1}{\rho c_p}(T - T_\infty) + \frac{\beta_1^* u}{\rho c_p}(T_\infty - T) + \frac{1}{c_p\rho}\frac{\partial q_r}{\partial y} + \tau\left[D_B\frac{\partial C}{\partial y}\frac{\partial T}{\partial y} + \frac{D_T}{T_\infty}\left(\frac{\partial T}{\partial y}\right)^2\right], \tag{20}$$

and

$$u\frac{\partial C}{\partial x} + v\frac{\partial C}{\partial y} = \frac{\partial^2 C}{\partial y^2}D_B + \frac{\partial^2 T}{\partial y^2}\frac{D_T}{T_\infty}. \tag{21}$$

The appropriate boundary constraints are given by

$$\begin{cases} u = a_1 x, \;\; v = v_w, \;\; T = T_w = T_\infty + A_0 x \\ C = C_w = B_0 x_\infty + C_\infty \quad at \quad y = 0 \\ u \longrightarrow 0, \quad C \longrightarrow C_\infty, \quad T \longrightarrow T_\infty \quad as \quad y \longrightarrow \infty. \end{cases} \tag{22}$$

Here, the velocity components are denoted by u and v along the x-axis and the y-axis, respectively, c_p is the specific heat, T is the temperature, B_0 is the applied magnetic induction, T_w is the wall temperature, β_1 is the coefficient of thermal expansion, a_1 is the stretching rate, g_1 is the acceleration due to gravity, v is the fluid kinematic viscosity, k_1^* is the mean absorption coefficient, ρ is the fluid density, v_w is the wall injection when $v_w > 0$ and the wall suction when ($v_w < 0$), σ is the electrical conductivity, $\beta_1^* u(T_\infty - T)$ and $Q_1(T - T_\infty)$ are the heat generation and absorption, where (β_1^* and Q_1 are constants) and σ_1^* is the Stefan Boltzmann constant. The first term on the right-hand side of Equations (19)–(21) represents the net force due to the viscous shear stress, the net inflow of thermal energy due to the y-direction conduction, and the net inflow due to the y-direction diffusion, respectively. In terms of the free stream function $\psi(x, y)$, the components of velocity are described as follows:

$$u = \frac{\partial \psi}{\partial y}, \quad v = -\frac{\partial \psi}{\partial x}. \tag{23}$$

For the similarity solutions, we use the following acceptable variable:

$$\eta = y\sqrt{\frac{a_1}{v}}, \quad \theta = \frac{T - T_\infty}{T_w - T_\infty}, \quad \psi(x,y) = \sqrt{va_1}xf(\eta), \quad \phi = \frac{C - C_\infty}{C_w - C_\infty}. \tag{24}$$

The heat flux q_r is calculated as follows:

$$q_r = -\frac{4\sigma_1^*}{3k_1^*}\frac{\partial T^4}{\partial y}. \tag{25}$$

Here, we have

$$T^4 \approx 4T_\infty^3 T - 3T_\infty^4, \tag{26}$$

upon inserting Equations (24)–(26) into Equations (19)–(21), we have

$$f''' + f'^2 + \theta G_r + ff'' - M^2 f' - f'^2 F_1 + f'k_1 = 0, \tag{27}$$

$$\frac{1}{Pr}(1 + \frac{4R}{3})\theta'' + \phi'^2 N_t + \theta' f + \theta'\phi' N_b + \Delta\theta - \delta_1\theta f' = 0, \tag{28}$$

and

$$\phi'' + \phi' f Sc + \theta''\frac{N_t}{N_b} = 0. \tag{29}$$

The dimensionless BCs are given

$$f(0) = -R_1,\ \theta(0) = 1,\ \phi(0) = 1,\ f'(0) = 1,\ f'(\infty) = 1,\ \phi(\infty) = 0,\ \theta(\infty) = 0. \tag{30}$$

The converging parameters involved in the foregoing Equations (27)–(30) are given below:

$$\begin{cases} F_1 = \frac{C_b}{\sqrt{k_0}}x, \quad N_t = \frac{\tau D_T(T_w - T_\infty)}{vT_\infty}, \quad k_1 = \frac{v}{k_0 a_1}, \quad N_b = \frac{\tau D_B(C_w - C_\infty)}{v}, \\ Sc = \frac{v}{D_B}, \quad M = (\frac{\sigma}{\rho a_1})^{\frac{1}{2}}B_0, \quad \delta_1 = \frac{\beta_1^* x}{\rho c_p}, \quad R = \frac{4\sigma_1^* T_\infty^3}{k_1^* k_0}, \quad Pr = \frac{v}{\alpha}, \\ G_r = g_1\beta_1\frac{(T_w - T_\infty)}{a_1^2 x}, \quad R_1 = \frac{v_w}{\sqrt{va_1}}, \quad \Delta = \frac{Q_1}{\rho c_p a_1}. \end{cases} \tag{31}$$

We explained detail formulation of all governing equations in Appendix A.

Physical Quantities

Some of the most important physical quantities in the engineering processes are Sh_x, Nu_x, and C_f, which are indicated below:

$$Sh_x = \frac{xq_m}{D_B(C_w - C_\infty)}, \quad Nu_x = \frac{xq_w}{k_f(T_w - T_\infty)}, \quad C_f = \frac{\tau_w}{\rho u_w^2}, \tag{32}$$

where

$$q_m = -D_B\left(\frac{\partial C}{\partial y}\right)_{y=0}, \quad q_w = -k_f\left(\frac{\partial T}{\partial y}\right)_{y=0}, \quad \tau_w = \mu\left(\frac{\partial u}{\partial y}\right)_{y=0}. \tag{33}$$

Using Equations (24) and (33) into Equation (32), we have

$$[Re]^{-\frac{1}{2}}Sh_x = -\phi'(0), \quad [Re]^{-\frac{1}{2}}Nu_x = -\theta'(0), \quad [Re]^{\frac{1}{2}}C_f = f''(0). \tag{34}$$

Here $Re = \frac{xu_w}{v}$ denotes the Reynolds number.

4. The HAM Solution

In order to determine an approximate solution for the dimensionless set of Equations (27)–(29) by incorporating the boundary condition as given in Equation (30), we shall apply the well-known homotopy analysis method (HAM) in the *Mathematica*

software. To employ this method, we need initial guesses for the approximate solutions to Equations (27)–(29). These initial guesses are presented as follows:

$$\begin{aligned} \phi_0(\eta) &= e^{-\eta}, \\ \theta_0(\eta) &= e^{-\eta}, \\ f_0(\eta) &= R_1 - e^{-\eta} + \eta. \end{aligned} \tag{35}$$

The linear operators $\mathscr{L}_\phi$, $\mathscr{L}_\theta$, and $\mathscr{L}_f$ are given below:

$$\begin{aligned} \mathscr{L}_\phi(\phi) &= \phi'', \\ \mathscr{L}_\theta(\theta) &= \theta'', \\ \mathscr{L}_f(f) &= f'''. \end{aligned} \tag{36}$$

The expanded forms of the linear operators in Equation (36) are given by

$$\begin{aligned} \mathscr{L}_\phi(c_1 + c_2\eta) &= 0, \\ \mathscr{L}_\theta(c_3 + c_4\eta) &= 0, \\ \mathscr{L}_f(c_5 + c_6\eta + c_7\eta^2) &= 0. \end{aligned} \tag{37}$$

In this last Equation (37), c_i $(i = 1, 2, \ldots, 7)$ are considered constant. Moreover, on the basis of Equation (35), the non-linear operators $\mathscr{N}_{\widehat{\phi}}$, $\mathscr{N}_{\widehat{\theta}}$, and $\mathscr{N}_{\widehat{f}}$ are given as follows:

$$\mathscr{N}_{\widehat{\phi}}\left[\widehat{\phi}(\eta;p), \widehat{\theta}(\eta;p), \widehat{f}(\eta;p)\right] = \widehat{\phi}_{\eta\eta} + (\widehat{f}_\eta\widehat{\phi} + \widehat{\phi}_\eta\widehat{f})Sc + \widehat{\theta}_{\eta\eta}\tfrac{N_t}{N_b}, \tag{38}$$

$$\begin{aligned} &\mathscr{N}_{\widehat{\theta}}\left[\widehat{\theta}(\eta;p), \widehat{\phi}(\eta;p), \widehat{f}(\eta;p)\right] \\ &\qquad = \frac{1}{Pr}\left(1 + \frac{4R}{3}\right)\widehat{\theta}_{\eta\eta} + \widehat{\phi}_\eta^2 N_t + \widehat{\theta}_\eta\widehat{f} + \widehat{\theta}_\eta\widehat{\phi}_\eta N_b + \Delta\widehat{\theta} - (1+\delta_1)\widehat{\theta}\widehat{f}_\eta, \end{aligned} \tag{39}$$

and

$$\mathscr{N}_{\widehat{f}}\left[\widehat{f}(\eta;p)\right] = \widehat{f}_{\eta\eta\eta} + \widehat{f}_\eta^2 + \widehat{\theta}G_r + \widehat{f}\widehat{f}_{\eta\eta} - M^2\widehat{f}_\eta - \widehat{f}_\eta^2 F_1 + \widehat{f}_\eta k_1. \tag{40}$$

The deformation equations that can be of the 0th order are listed as follows:

$$(1-p)\mathscr{L}_{\widehat{\phi}}[\widehat{\phi}(\eta;p) - \widehat{\phi}_0(\eta)] = p\hbar_{\widehat{\phi}}\mathrm{N}_{\widehat{\phi}}\left[\widehat{\phi}(\eta;p), \widehat{\theta}(\eta;p), \widehat{f}(\eta;p)\right], \tag{41}$$

$$(1-p)\mathscr{L}_{\widehat{\theta}}\left[\widehat{\theta}(\eta;p) - \widehat{\theta}_0(\eta)\right] = p\hbar_{\widehat{\theta}}\mathrm{N}_{\widehat{\theta}}\left[\widehat{\phi}(\eta;p), \widehat{\theta}(\eta;p), \widehat{f}(\eta;p)\right], \tag{42}$$

and

$$(1-p)\mathscr{L}_{\widehat{f}}\left[\widehat{f}(\eta;p) - \widehat{f}_0(\eta)\right] = p\hbar_{\widehat{f}}\mathrm{N}_{\widehat{f}}\left[\widehat{f}(\eta;p)\right]. \tag{43}$$

The BCs for Equations (41)–(43) are given by

$$\begin{aligned} &\widehat{f}(\eta;p)\Big|_{\eta=0} = -R_1, \quad \widehat{\theta}(\eta;p)\Big|_{\eta=0} = 1, \quad \widehat{\phi}(\eta;p)|_{\eta=0} = 1, \quad \tfrac{\partial\widehat{f}(\eta;p)}{\partial\eta}\Big|_{\eta=0} = 1, \\ &\tfrac{\partial\widehat{f}(\eta;p)}{\partial\eta}\Big|_{\eta=\infty} = 1, \quad \widehat{\theta}(\eta;p)\Big|_{\eta=\infty} = 0, \quad \widehat{\phi}(\eta;p)|_{\eta=\infty} = 0. \end{aligned} \tag{44}$$

Moreover, when $p = 0$ and $p = 1$, we have

$$\begin{aligned} \widehat{\phi}(\eta;0) &= \widehat{\phi_0}(\eta), \\ \widehat{\theta}(\eta;0) &= \widehat{\theta_0}(\eta), \\ \widehat{f}(\eta;0) &= \widehat{f_0}(\eta), \end{aligned} \tag{45}$$

and

$$\begin{aligned}\widehat{\phi}(\eta;1) &= \widehat{\phi}(\eta),\\ \widehat{\theta}(\eta;1) &= \widehat{\theta}(\eta),\\ \widehat{f}(\eta;1) &= \widehat{f}(\eta).\end{aligned} \tag{46}$$

Now, by using the Maclaurin expansion for $\widehat{\phi}(\eta;p)$, $\widehat{\theta}(\eta;p)$, and $\widehat{f}(\eta;p)$ at $p = 0$, we have

$$\begin{aligned}\widehat{\phi}(\eta;0) &= \widehat{\phi}_0(\eta) + \sum_{m=1}^{\infty} \widehat{\phi}_m(\eta)p^m,\\ \widehat{\theta}(\eta;0) &= \widehat{\theta}_0(\eta) + \sum_{m=1}^{\infty} \widehat{\theta}_m(\eta)p^m,\\ \widehat{f}(\eta;0) &= \widehat{f}_0(\eta) + \sum_{m=1}^{\infty} \widehat{f}_m(\eta)p^m.\end{aligned} \tag{47}$$

Here, we have

$$\begin{aligned}\widehat{\phi}_m(\eta) &= \left.\frac{1}{m!}\frac{\partial^n \widehat{\phi}(\eta;p)}{\partial p^n}\right|_{p=0},\\ \widehat{\theta}_m(\eta) &= \left.\frac{1}{m!}\frac{\partial^n \widehat{\theta}(\eta;p)}{\partial p^n}\right|_{p=0},\\ \widehat{f}_m(\eta) &= \left.\frac{1}{m!}\frac{\partial^n \widehat{f}(\eta;p)}{\partial p^n}\right|_{p=0}.\end{aligned} \tag{48}$$

The deformation equations that can be of the mth-order are defined as follows:

$$\mathscr{L}_{\widehat{\phi}}\left[\widehat{\phi}_m(\eta) - \chi_m\widehat{\phi}_{m-1}(\eta)\right] = \hbar_{\widehat{\phi}}\mathfrak{R}_m^{\widehat{\phi}}(\eta), \tag{49}$$

$$\mathscr{L}_{\widehat{\theta}}\left[\widehat{\theta}_m(\eta) - \chi_m\widehat{\theta}_{m-1}(\eta)\right] = \hbar_{\widehat{\theta}}\mathfrak{R}_m^{\widehat{\theta}}(\eta), \tag{50}$$

and

$$\mathscr{L}_{\widehat{f}}\left[\widehat{f}_m(\eta) - \chi_m\widehat{f}_{m-1}(\eta)\right] = \hbar_{\widehat{f}}\mathfrak{R}_m^{\widehat{f}}(\eta). \tag{51}$$

together with the BCs given by

$$\widehat{\phi}(0) = 1,\ \widehat{f}(0) = -R_1,\ \widehat{\theta}(0) = 1,\ \widehat{f}'(0) = 1,\ \widehat{f}'(\infty) = 1,\ \widehat{\theta}(\infty) = 0,\ \widehat{\phi}(\infty) = 0. \tag{52}$$

5. Results and Discussion

Here, in this section, we shall discuss the convergence of the above-derived solution. The analytical solution includes the convergence control parameter $\hbar$, which can affect the rate of approximation and the converging regions for the HAM solutions. The constant $\hbar$ curve is quite rational whenever convergence takes place at $p = 1$. The convergence of Equations (41)–(43) is completely particularized by the secondary restriction $\hbar_f$, $\hbar_\theta$, and $\hbar_\phi$. There was a choice to control the series solutions and achieve their convergence. The probabilities of $\hbar$ are represented by the $\hbar$ curve for the fifth-order computed HAM solution. The efficient regions of $\hbar$ are $-2.0 < \hbar_f < 1.0$, $-4.0 < \hbar_\theta < 1.0$ and $-3.0 < \hbar_\phi < 1.0$. The convergence of the homotopy analysis method by the $\hbar$ curve was employed for $f''(0)$, $\theta'(0)$ and $\phi'(0)$, as demonstrated in Figures 2–4.

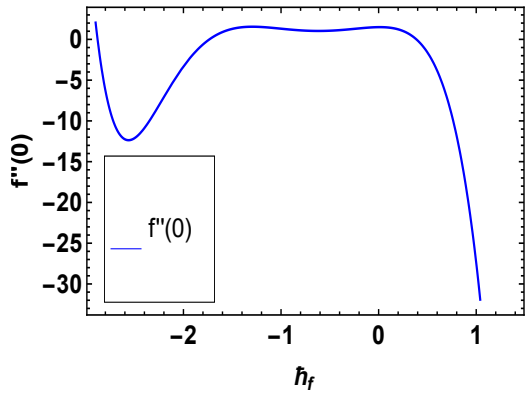

Figure 2. Outcomes of $\hbar_f$ for $f''(0)$.

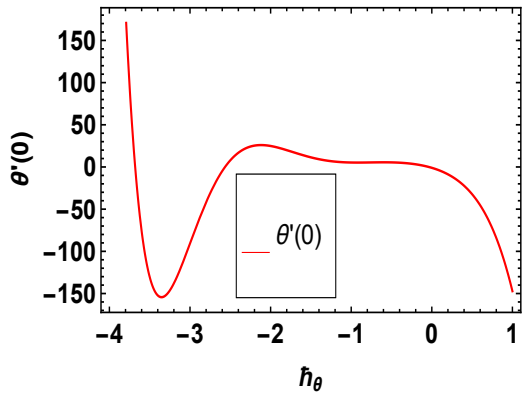

Figure 3. Outcomes of $\hbar_\theta$ for $\theta'(0)$.

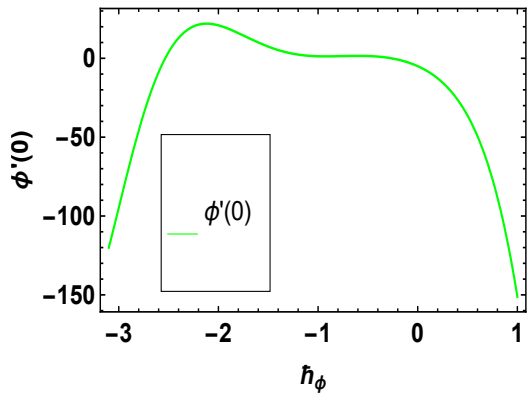

Figure 4. Outcomes of $\hbar_\phi$ for $\phi'(0)$.

5.1. Velocity Profile

The important characteristics of the flow profile are graphically displayed in this subsection for certain embedded parameters, such as the magnetic parameter, the inertial parameter, the porosity parameter, and the Grashof number. Figures 5–8 represent the impact of $f'(\eta)$, which is displayed, respectively, for varying rates of M, F_1, k_1, and G_r. Figure 5 characterizes the results of $f'(\eta)$ for the dissimilar rate of M when G_r = 2.0, k_1 = 0.4, and F_1 = 0.5. From this graph, we predict that $f'(\eta)$ is dropped with the rising of M. Physically, the magnetic effects create drag forces, which produce resistance and can slow down the fluid motion, thereby reducing $f'(\eta)$. Figure 6 characterizes the result of $f'(\eta)$ for the dissimilar rate of F_1 when G_r = 2.0, N_t = 0.6, k_1 = 0.4, and M = 0.8. It can be observed from Figure 6 that the $f'(\eta)$ curves are reduced against the rising of the values of F_1. The inertial factor is directly proportional to the drag coefficient and

porous medium. Thus, for high values of F_1, both the drag coefficients and porosity of the medium rise. Consequently, a resisting force is boosted and, therefore, lower velocity is obtained, corresponding to bigger values of F_1. Figure 7 depicts the variations of $f'(\eta)$ for various values of k_1 when $G_r = 2.0$, $N_b = 0.4$, $F_1 = 0.5$, and $M = 0.8$. This curve shows that $f'(\eta)$ decreases for some rising values of k_1. Porous medium boosted the resistance to the fluid motion. Since the free convection Reynolds number is not an independent parameter and the heat transfer coefficients are small, a new dimensionless grouping of the Grashof number plays an important role, which incorporates the coefficients of the thermal expansion β_1 in the formulation. Figure 8 depicts the behavior of $f'(\eta)$ for varying values of G_r when $k_1 = 0.4$, $Sc = 0.3$, $F_1 = 0.5$, and $M = 0.8$. This figure shows that $f'(\eta)$ increases for larger rates of G_r. The Grashof number is a measurement of the ratio of the buoyancy force to the viscous force operating on the fluid.

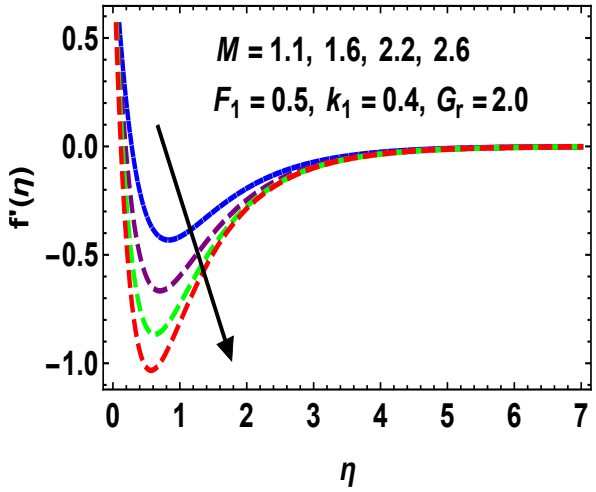

Figure 5. Outcomes of $f'(\eta)$ for M where blue, purple, green, and red lines represent for $M = 1.1$, $M = 1.6$, $M = 2.2$, and $M = 2.6$ respectively.

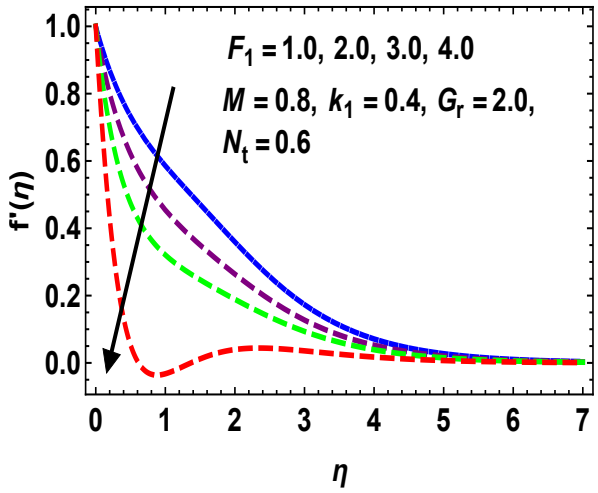

Figure 6. Outcomes of $f'(\eta)$ for F_1 where blue, purple, green, and red lines represent for $F_1 = 1.0$, $F_1 = 2.0$, $F_1 = 3.0$, and $F_1 = 4.0$ respectively.

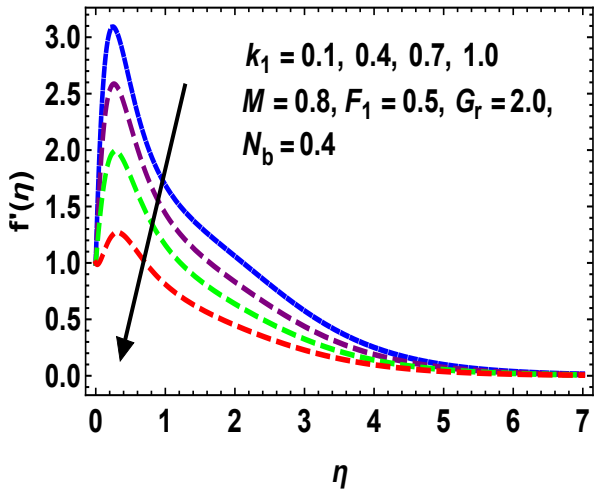

Figure 7. Outcomes of $f'(\eta)$ for k_1 where blue, purple, green, and red lines represent for $k_1 = 0.1$, $k_1 = 0.4$, $k_1 = 0.7$, and $k_1 = 1.0$ respectively.

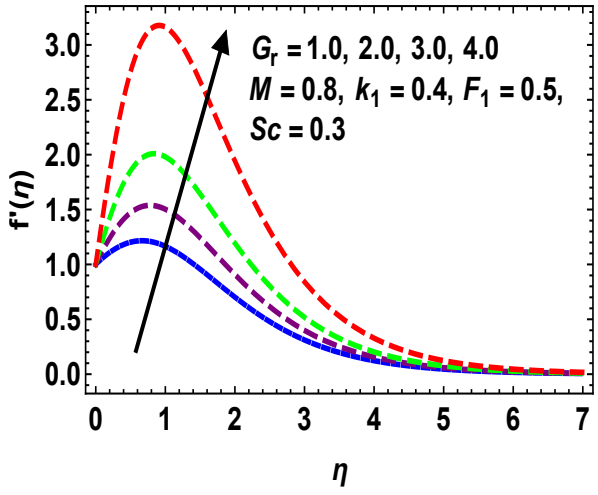

Figure 8. Outcome of $f'(\eta)$ for G_r where blue, purple, green, and red lines represent for $G_r = 1.0$, $G_r = 2.0$, $G_r = 3.0$, and $G_r = 4.0$ respectively.

5.2. Thermal and Concentration Profiles

The important characteristics of the thermal and concentration properties are graphically displayed in this subsection for certain embedded parameters, such as the Brownian motion parameter, the thermophoresis parameter, the radiation parameter, the heat generation/absorption parameter, the Prandtl number, and the Schmidt number. Figures 9–17 show the impact of $\theta(\eta)$ and $\phi(\eta)$, which are, respectively, plotted for certain values of Δ, N_b, N_t, R, Pr, and Sc. The behavior of the heat source $(\Delta > 0)$ or the heat sink parameter $(\Delta < 0)$ on $\theta(\eta)$ has been analyzed in Figures 9 and 10. From these figures, it is recognized that the heat source $(\Delta > 0)$ enhanced the heat transfer variation. This enhancement in the temperature of the fluid causes the greatly-induced flow toward the plates through the buoyancy impact. Moreover, the figures show that the heat sink parameter $(\Delta < 0)$ declines $\theta(\eta)$. This decline in $\theta(\eta)$ causes a reduction in the boundary layer flow, which is the result of the buoyancy impact on the thermal problem. Figures 11 and 12 elaborate on the effects of N_b on $\theta(\eta)$ when $N_t = 0.7$, $Pr = 2.5$, $R = 1.3$ and $\phi(\eta)$ when $N_t = 0.7$ and $Sc = 0.4$. These results recognize that $\theta(\eta)$ is enhanced for bigger values of N_b, whereas the reverse trend is noted for $\phi(\eta)$. Figures 13 and 14 indicate the effects of N_t on $\theta(\eta)$ whenever $N_b = 0.6$, $Pr = 2.7$, $R = 1.6$, and $\phi(\eta)$ whenever $N_b = 0.6$ and $Sc = 0.4$. Due to the enhancement in the thermophoretic parameter, the thermophoresis force is enhanced,

which helps the fluid to migrate from the heated location to the cooler one. Thus, clearly, $\theta(\eta)$ and $\phi(\eta)$ are enhanced for higher rates of N_t. Figure 15 indicates the behavior of R on $\theta(\eta)$. It is necessary to keep in mind that more of an estimation of R strengthens $\theta(\eta)$ because the radiation factor produces thermal energy in the flow regions. Therefore, increments have been observed in $\theta(\eta)$. The behavior of Pr on $\theta(\eta)$ is exhibited in Figure 16. From this graph, we conclude that an increase in Pr declines the $\theta(\eta)$ curves. The physical interpretations of the Prandtl number follow its definition as a ratio of the momentum diffusivity to the thermal diffusivity. It is common in the problem of heat transfer that Pr is utilized to reduce the relative thickness of the momentum and the thermal boundary layers. Figure 17 indicates that there is a reduction in $\phi(\eta)$ for Sc = 0.5, 1.2, 1.8, and 2.4 when N_t = 1.2 and N_b = 1.4. Physically, the Schmidt number provides the measurement of the relative effectiveness of the mass and momentum transport by diffusion in the concentration and the velocity boundary layer.

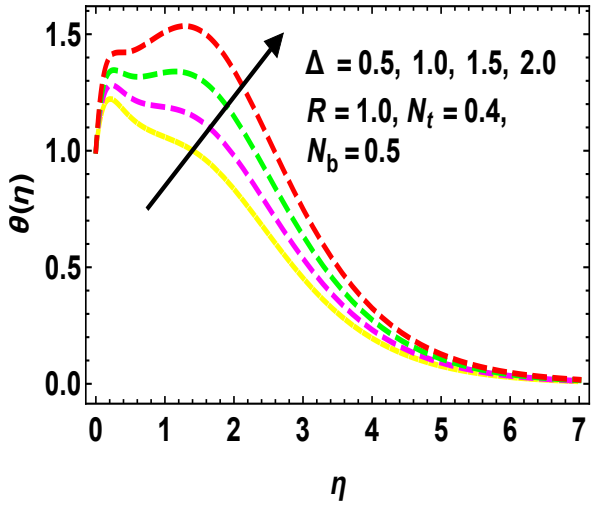

Figure 9. Outcomes of $\theta(\eta)$ for $\Delta > 0$ where yellow, magenta, green, and red lines represent for Δ = 0.5, Δ = 1.0, Δ = 1.5, and Δ = 2.0 respectively.

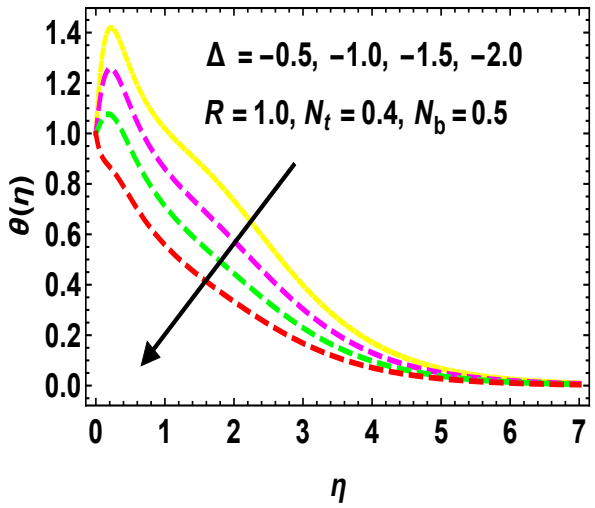

Figure 10. Outcomes of $\theta(\eta)$ for $\Delta < 0$ where yellow, magenta, green, and red lines represent for $\Delta = -0.5$, $\Delta = -1.0$, $\Delta = -1.5$, and $\Delta = -2.0$ respectively.

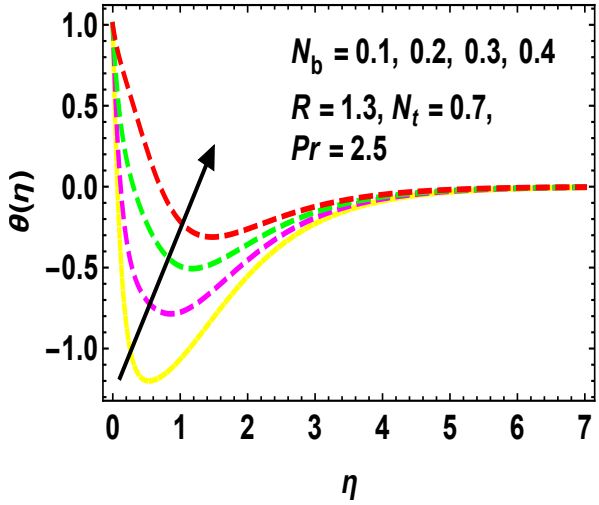

Figure 11. Outcomes of $\theta(\eta)$ for N_b where yellow, magenta, green, and red lines represent for $N_b = 0.1$, $N_b = 0.2$, $N_b = 0.3$, and $N_b = 0.4$ respectively.

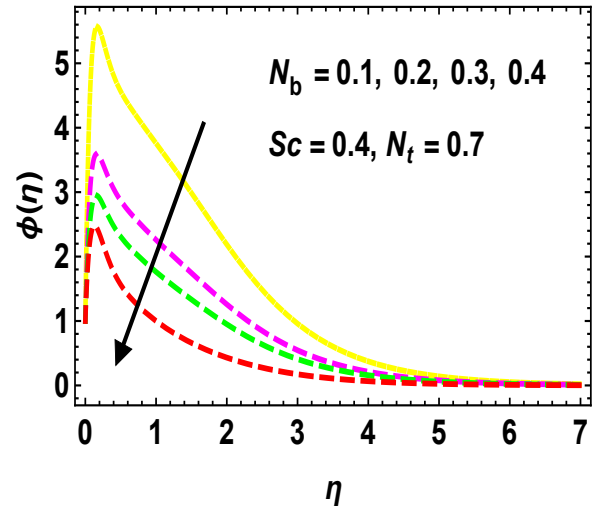

Figure 12. Outcomes of $\phi(\eta)$ for N_b where yellow, magenta, green, and red lines represent for $N_b = 0.1$, $N_b = 0.2$, $N_b = 0.3$, and $N_b = 0.4$ respectively.

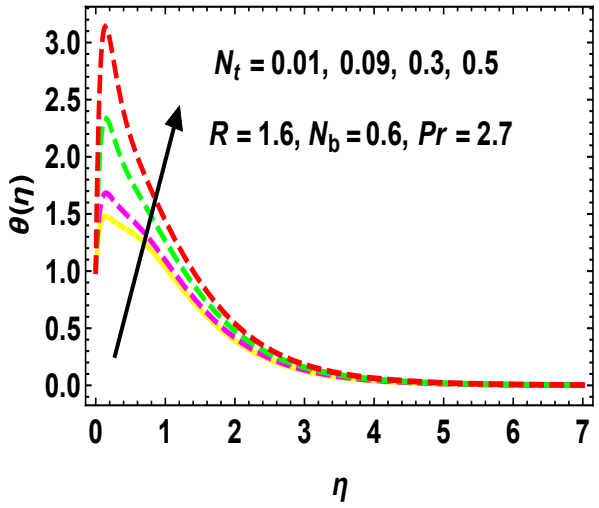

Figure 13. Outcomes of $\theta(\eta)$ for N_t where yellow, magenta, green, and red lines represent for $N_t = 0.01$, $N_t = 0.09$, $N_t = 0.3$, and $N_t = 0.5$ respectively.

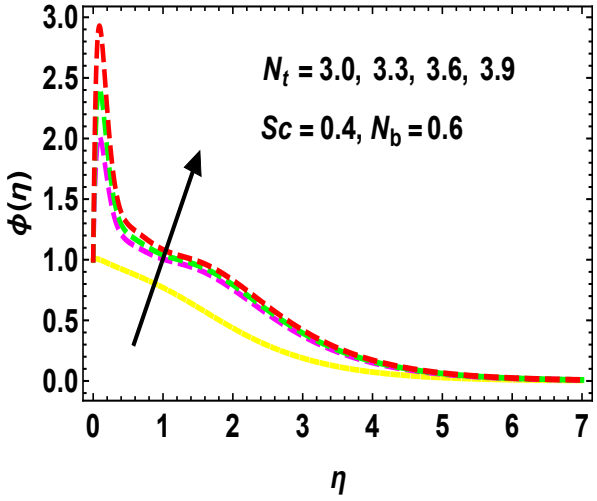

Figure 14. Outcomes of $\phi(\eta)$ for N_t where yellow, magenta, green, and red lines represent for N_t = 3.0, N_t = 3.3, N_t = 3.6, and N_t = 3.9 respectively.

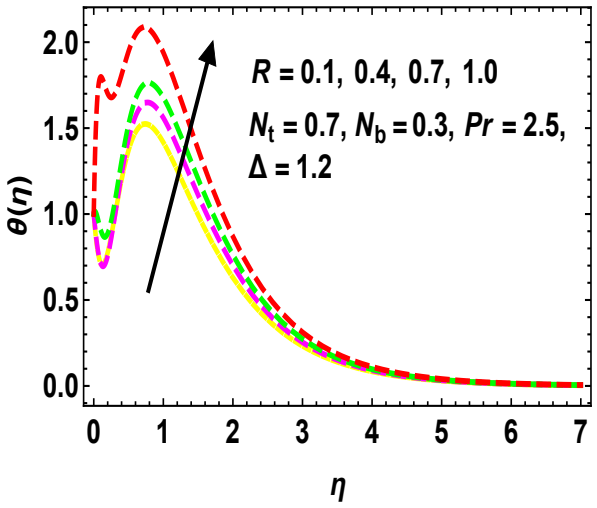

Figure 15. Outcomes of $\theta(\eta)$ for R where yellow, magenta, green, and red lines represent for R = 0.1, R = 0.4, R = 0.7, and R = 1.0 respectively.

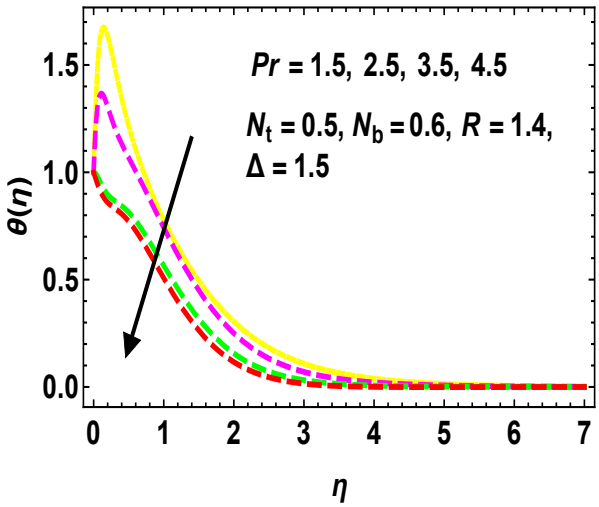

Figure 16. Outcomes of $\theta(\eta)$ for Pr where yellow, magenta, green, and red lines represent for Pr = 1.5, Pr = 2.5, Pr = 3.5, and Pr = 4.5 respectively.

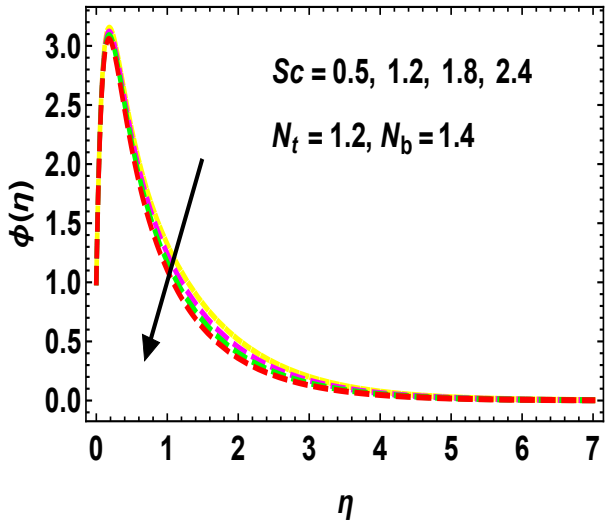

Figure 17. Outcomes of $\phi(\eta)$ for Sc where yellow, magenta, green, and red lines represent for Sc = 0.5, Sc = 1.2, Sc = 1.8, and Sc = 2.4 respectively.

5.3. Table Discussions

Our discussions on the numerical outcomes of Sh_x, C_f, and Nu_x for different convergence factors, such as F_1, k_1, M, G_r, R, Pr, N_t, N_b, and Sc are exhibited in Tables 1–3. Table 1 indicates the numerical outcomes of Sh_x for N_t = 0.2, 0.4, 0.6, 0.8, N_b = 0.1, 0.3, 0.5, 0.7, and Sc = 0.3, 0.5, 0.7, 0.9. The result of Sh_x is enhanced for a greater estimation of N_t and Sc while Sh_x diminishes for the rising credit of N_b. It is clearly depicted from Table 2 that C_f boots up for higher rates of F_1, k_1 and M, whereas the opposite behavior is seen for higher values of G_r. The variations of Pr, N_t, N_b, and R upon Nu_x are discussed in Table 3. It is clearly observed from Table 3 that Nu_x increases for more increments of R, N_b, and N_t, while it reduces for higher values of Pr. Furthermore, Table 4 represents the comparison of $-\theta'(0)$ for several values of R_1 and δ_1 by using HAM with the results by Daniel [49] and Chamkha [50]. It can also be observed from Table 4 that the obtained results are in close agreement with those published in the earlier investigations.

Table 1. Numerical outcomes of Sh_x for N_t, N_b and Sc.

N_t	N_b	Sc	Sh_x
0.2	0.1	0.3	2.45038307
0.4			2.36012785
0.6			2.34056085
0.8			2.31059187
	0.1		2.26205129
	0.3		2.27140738
	0.5		2.29025809
	0.7		2.29506702
		0.3	2.46230876
		0.5	2.45037182
		0.7	2.44570887
		0.9	2.42071925

Table 2. Numerical outcomes of C_f for k_1, M, G_r, and F_1.

F_1	k_1	M	G_r	C_f
0.3	0.1	0.3	1.0	1.63205892
0.4				1.64218038
0.5				1.64575398
0.6				1.66094124
	0.1			1.23056802
	0.2			1.24059735
	0.3			1.25192114
	0.4			1.25602565
		0.3		1.43271729
		0.5		1.45952172
		0.8		1.47062175
		1.0		1.48073426
			1.0	2.03968538
			2.0	1.90250917
			3.0	1.86620846
			4.0	1.80911127

Table 3. Numerical outcomes of Nu_x for R, Pr, N_t, and N_b.

R	Pr	N_t	N_b	Nu_x
0.5	2.5	0.1	0.2	2.53802156
1.0				2.52508295
1.2				2.51862063
1.5				2.50752047
	2.5			1.54531398
	3.5			1.59370589
	4.5			1.64950842
	5.5			1.66097014
		0.2		1.10459009
		0.4		1.02054179
		0.6		0.85628206
		0.8		0.80049531
			0.3	1.27353338
			0.5	1.25904107
			0.7	1.23718056
			0.9	1.21562169

Table 4. Comparison of $-\theta'(0)$ for R_1 and δ_1.

R_1	δ_1	Daniel [49]	Chamkha [50]	Present Study
0	0.5	0.94765	0.94769	0.94661
0	1.0	1.07895	1.07996	1.07713
0.45	0.5	0.82396	0.82397	0.82238
0.45	1.0	0.96190	0.96191	0.96052
−1.5	0.5	1.57077	1.57077	1.57061
−1.5	1.0	1.66182	1.66184	1.66047

6. Concluding Remarks

In this study, we proposed a mathematical model in order to investigate how radiation and buoyancy affect the MHD 2D boundary layer's fluid flow across a stretchable porous sheet. The flow of fluid is considered laminar, incompressible, and electrically conducted. The behavior of thermophoresis, heat source, sink, and the Brownian motion were systematically investigated in this work. The general form of the buoyancy term in the momentum equation for a free convection boundary layer is derived if the flow is due to temperature variations. The results, which we presented in this work, are shown to match with those

in the earlier published studies and are found to be in remarkable agreement. Before solving the modeled problem, similarity variables were utilized to convert the fundamental governing PDEs into the corresponding ODEs. A semi-analytical HAM approach was then applied for solving Equations (27)–(29) with the boundary conditions in Equation (30). The analysis was carried out up to the fifth-order HAM approximation solution.

The core findings of this work are summarized as follows:

- $f'(\eta)$ increased for high values of G_r and decreased for the increment values of k_1, F_1, and M.
- $\theta(\eta)$ enhances with the rising rates of $(\Delta > 0)$, N_b, R, and N_t, and diminishes with higher Pr and negative values of Δ.
- For more estimations of N_t, there is an increment in the $\phi(\eta)$ curves.
- $\phi(\eta)$ gradually diminishes against higher values of Sc and N_b.
- Higher estimations of M, F_1, and k_1 upsurge C_f, whereas the reverse is seen for G_r.
- Nu_x enhances due to increments of N_t, R and N_b, while it reduces due to higher Pr values.
- Sh_x reduces due to greater estimation of N_b and decreases for higher values of N_t and Sc.
- The role of the Grashof number is the same in free convection as that of the Reynolds number in the forced convection.

Author Contributions: Conceptualization, H.M.S., P.O.M., E.A.-S. and R.J.; data curation, M.J.; formal analysis, M.J.; funding acquisition, E.A.-S. and M.J.; investigation, H.M.S., Z.K., P.O.M., E.A.-S. and R.J.; methodology, Z.K., E.A.-S. and M.J.; project administration, H.M.S., P.O.M. and R.J.; resources, Z.K. and R.J.; software, Z.K. and P.O.M.; supervision, H.M.S., P.O.M. and R.J.; validation, M.J.; visualization, R.J.; writing—original draft, H.M.S., Z.K. and P.O.M.; writing—review and editing, E.A.-S. and M.J. All authors have read and agreed to the published version of the manuscript.

Funding: This research received no external funding.

Data Availability Statement: Not applicable.

Conflicts of Interest: The authors declare no conflict of interest.

Nomenclature

$B_0(x)$	applied magnetic induction
a_1	stretching rate
N_t	thermophoresis parameter
v, u	velocity components along y and x direction (ms^{-1})
T	fluid temperature (K)
β_1	thermal expansion
η	similarity variable
ψ	stream function (m^2s^{-1})
T_∞	free stream temperature (K)
ρ	fluid density (kgm^{-3})
g_1	acceleration due to gravity
σ_1^*	Boltzmann constant ($Wm^{-2}K^{-4}$)
c_p	specific heat ($Jm^{-3}K^{-1}$)
σ	electrical conductivity
δ_1	heat generation/absorption
α	thermal diffusivity
M	magnetic parameter
k_1^*	mean absorption coefficient
T_w	wall temperature (K)
k_1	porosity parameter
R	radiation parameter
υ	kinematic viscosity (m^2s^{-1})
$\hbar$	convergence control parameter

F_1	inertia parameter
Δ	heat source/sink parameter
Re	Reynolds number
G_r	Grashof number
$\mathscr{L}_1$	auxiliary linear-operator
Sc	Schmidt number
q_r	heat flux
Pr	Prandtl number
R_1	suction/injection parameter
$\mathscr{N}_1$	non-linear operator
N_b	Brownian motion parameter

Appendix A. Derivation of the Flow Problem

The flow problem has the following governing equations and boundary conditions:
Continuity equation:

$$\frac{\partial u}{\partial x} + \frac{\partial v}{\partial y} = 0 \tag{A1}$$

Momentum equation:

$$u\frac{\partial u}{\partial x} + v\frac{\partial u}{\partial y} = v\frac{\partial^2 u}{\partial y^2} - \frac{\sigma B_0^2(x)}{\rho}u + g_1\beta_1(T - T_\infty) - u\frac{v}{k_0} - F_0u^2 \tag{A2}$$

Energy equation:

$$u\frac{\partial T}{\partial x} + v\frac{\partial T}{\partial y} = \alpha\frac{\partial^2 T}{\partial y^2} + \frac{Q_1}{\rho c_p}(T - T_\infty) + \frac{\beta_1^* u}{\rho c_p}(T_\infty - T) + \frac{1}{c_p\rho}\frac{\partial q_r}{\partial y} + \tau\left[D_B\frac{\partial C}{\partial y}\frac{\partial T}{\partial y} + \frac{D_T}{T_\infty}\left(\frac{\partial T}{\partial y}\right)^2\right] \tag{A3}$$

Concentration equation:

$$u\frac{\partial C}{\partial x} + v\frac{\partial C}{\partial y} = \frac{\partial^2 C}{\partial y^2}D_B + \frac{\partial^2 T}{\partial y^2}\frac{D_T}{T_\infty}. \tag{A4}$$

Boundary constraints:

$$\begin{cases} u = a_1x, \;\; v = v_w, \;\; T = T_w = T_\infty + A_0x \\ C = C_w = B_0x_\infty + C_\infty \quad at \quad y = 0 \\ u \longrightarrow 0, \quad C \longrightarrow C_\infty, \quad T \longrightarrow T_\infty \quad as \quad y \longrightarrow \infty. \end{cases} \tag{A5}$$

The dimensionless variables are given as

$$\eta = y\sqrt{\frac{a_1}{v}}, \;\; \theta = \frac{T - T_\infty}{T_w - T_\infty}, \;\; \psi(x,y) = \sqrt{va_1}xf(\eta), \;\; \phi = \frac{C - C_\infty}{C_w - C_\infty}. \tag{A6}$$

Appendix A.1. Derivation of the Continuity Equation

From

$$u = \frac{\partial \psi}{\partial y} = \frac{\partial}{\partial y}(\sqrt{va_1}xf(\eta)) = a_1xf'(\eta) \tag{A7}$$

and

$$v = -\frac{\partial \psi}{\partial x} = -\sqrt{va_1}f(\eta), \tag{A8}$$

now

$$\frac{\partial u}{\partial x} = \frac{\partial}{\partial x}(a_1xf'(\eta)) = a_1f'(\eta) \tag{A9}$$

$$\frac{\partial v}{\partial y} = \frac{\partial}{\partial y}(-\sqrt{va_1}f(\eta)) = -a_1 f'(\eta). \tag{A10}$$

Substitute Equations (A9) and (A10) into Equation (A1), we have

$$\frac{\partial u}{\partial x} + \frac{\partial v}{\partial y} = a_1 f'(\eta) - a_1 f'(\eta) = 0. \tag{A11}$$

Thus, it satisfies the continuity equation.

Appendix A.2. Derivation of the Momentum Equation

$$u\frac{\partial u}{\partial x} = {a_1}^2 x f'^2 \tag{A12}$$

$$v\frac{\partial u}{\partial y} = -{a_1}^2 x f f'' \tag{A13}$$

$$v\frac{\partial^2 u}{\partial y^2} = {a_1}^2 x f''' \tag{A14}$$

$$-\frac{\sigma B_0^2(x)}{\rho}u = -\frac{\sigma B_0^2(x)}{\rho}a_1 x f'(\eta) \tag{A15}$$

$$-\frac{v}{k_0}u = -\frac{v}{k_0}a_1 x f'(\eta) \tag{A16}$$

$$-F_0 u^2 = -F_0 {a_1}^2 x^2 f'^2. \tag{A17}$$

Substituting Equation (A12) to Equation (A17) into Equation (A2), we have

$$f''' + f'^2 + \theta G_r + f f'' - M^2 f' - f'^2 F_1 + f' k_1 = 0, \tag{A18}$$

Appendix A.3. Derivation of the Energy Equation

$$u\frac{\partial T}{\partial x} = 0 \tag{A19}$$

$$v\frac{\partial T}{\partial y} = -a_1(T_w - T_\infty) f\theta' \tag{A20}$$

$$\alpha\frac{\partial^2 T}{\partial y^2} = \alpha(T_w - T_\infty)\theta''\frac{a_1}{v} \tag{A21}$$

$$\frac{Q_1}{\rho c_p}(T - T_\infty) = \frac{Q_1}{\rho c_p}(T_w - T_\infty)\theta \tag{A22}$$

$$-\frac{1}{c_p\rho}\frac{16\sigma_1^* T_\infty^3}{3k_1^*}\frac{\partial^2 T}{\partial y^2} = -\frac{1}{c_p\rho}\frac{16\sigma_1^* T_\infty^3}{3k_1^*}(T_w - T_\infty)\theta''\frac{a_1}{v} \tag{A23}$$

Substituting Equation (A19) to Equation (A23) into Equation (A3), we have

$$\frac{1}{Pr}(1 + \frac{4R}{3})\theta'' + \phi'^2 N_t + \theta' f + \theta'\phi' N_b + \Delta\theta - \delta_1\theta f' = 0, \tag{A24}$$

Appendix A.4. Derivation of Concentration Equation

$$u\frac{\partial C}{\partial x} = 0 \tag{A25}$$

$$v\frac{\partial C}{\partial y} = -a_1(C_w - T_\infty) f\phi' \tag{A26}$$

$$D_B \frac{\partial^2 C}{\partial y^2} = D_B (C_w - T_\infty) \phi'' \frac{a_1}{v} \tag{A27}$$

$$\frac{D_T}{T_\infty} \frac{\partial^2 T}{\partial y^2} = \frac{D_T}{T_\infty} (T_w - T_\infty) \theta'' \frac{a_1}{v}. \tag{A28}$$

Substituting Equation (A25) to Equation (A28) into Equation (A4), we have

$$\phi'' + \phi' f Sc + \theta'' \frac{N_t}{N_b} = 0. \tag{A29}$$

Appendix A.5. Derivation of Boundary Conditions

The derivation of boundary conditions at $\eta = 0$ and $\eta = \infty$ is as follows:

$$u = a_1 x$$
$$a_1 x f'(\eta) = a_1 x$$
$$f'(0) = 1$$

$$u = 0 \quad as \quad y \longrightarrow \infty$$
$$a_1 x f'(\infty) = 0$$
$$f'(\infty) = 0$$

$$v = v_w$$
$$-\sqrt{v a_1} f(\eta) = R_1 \sqrt{v a_1}$$
$$f(0) = -R_1$$

$$T = T_\infty \quad as \quad y \longrightarrow \infty$$
$$T - T_\infty = 0$$
$$(T_w - T_\infty)\theta = 0$$
$$\theta(\infty) = 0$$

$$T = T_\infty + A_1 x$$
$$T - T_\infty = \frac{T_w - T_\infty}{x} x$$
$$(T_w - T_\infty)\theta(0) = T_w - T_\infty$$
$$\theta(0) = 1$$

$$C = C_\infty \quad as \quad y \longrightarrow \infty$$
$$\phi(\infty) = 0$$
$$C - C_\infty = B_0 x$$
$$C - C_\infty = \frac{(C_w - C_\infty)}{x} x$$
$$(C_w - C_\infty)\phi(0) = (C_w - C_\infty)$$
$$\phi(0) = 1$$

References

1. Chaudhary, S.; Kumar, P. Unsteady magnetohydrodynamic boundary layer flow near the stagnation point towards a shrinking surface. *J. Appl. Math. Phys.* **2015**, *3*, 921–930. [CrossRef]
2. Naramgari, S.; Sulochana, C. MHD flow over a permeable stretching/shrinking sheet of a nanofluid with suction/injection. *Alex. Eng. J.* **2016**, *55*, 819–827. [CrossRef]
3. Reddy, G.V.R.; Reddy, N.B.; Gorla, R.S.R. Radiation and chemical reaction effects on MHD flow along a moving vertical porous plate. *Int. J. Appl. Mech. Eng.* **2016**, *21*, 157–168. [CrossRef]
4. Mishra, S.R.; Jena, S. Numerical solution of boundary layer MHD flow with viscous dissipation. *Sci. World J.* **2014**, *2014*, 756498. [CrossRef]
5. Babu, P.R.; Rao, J.A.; Sheri, S. Radiation effect on MHD heat and mass transfer flow over a shrinking sheet with mass suction. *J. Appl. Fluid Mech.* **2014**, *7*, 641–650. [CrossRef]
6. Mabood, F.; Khan, W.A.; Ismail, A.M. MHD flow over exponential radiating stretching sheet using homotopy analysis method. *J. King Saud Univ. Eng. Sci.* **2017**, *29*, 68–74. [CrossRef]
7. Pal, D.; Mondal, H. Effect of variable viscosity on MHD non-Darcy mixed convective heat transfer over a stretching sheet embedded in a porous medium with non-uniform heat source/sink. *Commun. Nonlinear. Sci. Numer. Simul.* **2010**, *15*, 1553–1564. [CrossRef]
8. Zeeshan, A.; Ellahi, R.; Hassan, M. Magnetohydrodynamic flow of water/ethylene glycol based nanofluids with natural convection through a porous medium. *Eur. Phys. J. Plus* **2014**, *129*, 261. [CrossRef]
9. Mahmoud, M.A.A. Variable viscosity effects on hydromagnetic boundary. *Appl. Math. Sci.* **2017**, *1*, 799–814.
10. Kishore, P.M.; Rajesh, V.; Verma, V.S. The effects of thermal radiation and viscous dissipation on MHD heat and mass diffusion flow past an oscillating vertical plate embedded in a porous medium with variable surface conditions. *Theor. Appl. Mech.* **2012**, *39*, 99–125. [CrossRef]
11. Majeed, A.; Noori, F.M.; Zeeshan, A.; Mahmood, T.; Rehman, S.U.; Khan, I. Analysis of activation energy in magnetohydrodynamic flow with chemical reaction and second order momentum slip model. *Case Stud. Therm. Eng.* **2018**, *12*, 765–773. [CrossRef]
12. Sharma, R.; Ishak, A.; Nazar, R.; Pop, I. Boundary layer flow and heat transfer over a permeable exponentially shrinking sheet in the presence of thermal radiation and partial slip. *J. Appl. Fluid Mech.* **2014**, *7*, 125–134. . [CrossRef]
13. Poornima, T.; Reddy, N.B. Radiation effects on mhd free convective boundary layer flow of nanofluids over a nonlinear stretching sheet. *Adv. Appl. Sci. Res.* **2013**, *4*, 190–202.
14. Singh, P.; Jangid, A.; Tomer, N.S.; Sinha, D. Effects of thermal radiation and magnetic field on unsteady stretching permeable sheet in presence of free stream velocity. *Int. J. Phys. Math. Sci.* **2010**, *4*, 396–402.
15. Ahmad, I.; Sajid, M.; Awan, W.; Rafique, M.; Aziz, W.; Ahmed, M.; Abbasi, A.; Taj, M. MHD flow of a viscous fluid over an exponentially stretching sheet in a porous medium. *J. Appl. Math.* **2014**, *2014*, 256761. [CrossRef]
16. Shateyi, S.; Motsa, S.S. Thermal radiation effects on heat and mass transfer over an unsteady stretching surface. *Math. Probl. Eng.* **2009**, *2009*, 965603. [CrossRef]
17. Waheed, S.E. Flow and heat transfer in a maxwell liquid film over an unsteady stretching sheet in a porous medium with radiation. *SpringerPlus* **2016**, *5*, 1061. [CrossRef]
18. Khan, A.S.; Nie, Y.; Shah, Z. Impact of thermal radiation on magnetohydrodynamic unsteady thin film flow of Sisko fluid over a stretching surface. *Process* **2016**, *7*, 369. [CrossRef]
19. Metri, P.G.; Tawade, J.; Abel, M.S. Thin film flow and heat transfer over an unsteady stretching sheet with thermal radiation. *arXiv* **2016**, arXiv:1603.03664.
20. Khan, Z.; Srivastava, H.M.; Mohammed, P.O.; Jawad, M.; Jan, R.; Nonlaopon, K. Thermal boundary layer analysis of MHD nanofluids across a thin needle using non-linear thermal radiation. *Math. Biosci. Eng.* **2022**, *19*, 14116–14141. [CrossRef]
21. Garia, R.; Rawat, S.K.; Kumar, M.; Yaseen, M. Hybrid nanofluid flow over two different geometries with Cattaneo–Christov heat flux model and heat generation: A model with correlation coefficient and probable error. *Chin. J. Phys.* **2021**, *74*, 421–439. [CrossRef]
22. Garia, R.; Rawat, S.K.; Kumar, M.; Yaseen, M. Cattaneo–Christov heat flux model in Darcy–Forchheimer radiative flow of MoS_2–SiO_2/kerosene oil between two parallel rotating disks. *J. Therm. Anal. Calorim.* **2022**, *147*, 10865–10887. [CrossRef]
23. Khan, Z.; Jawad, M.; Bonyah, E.; Khan, N.; Jan, R. Magnetohydrodynamic thin film flow through a porous stretching sheet with the impact of thermal radiation and viscous dissipation. *Math. Probl. Eng.* **2022**, *2022*, 1086847. [CrossRef]
24. Jawad, M.; Khan, Z.; Bonyah, E.; Jan, R. Analysis of hybrid nanofluid stagnation point flow over a stretching surface with melting heat transfer. *Math. Probl. Eng.* **2022**, *2022*, 9469164. [CrossRef]
25. Dullien, F.A.L. *Porous Media*: *Fluid Transport and Pore Structure*, 2nd ed.; Academic Press: New York, NY, USA; London, UK; San Diego, CA, USA, 2012.
26. Nield, D.A.; Bejan, A. *Convection in Porous Media*, 5th ed.; Springer: Berlin/Heidelberg, Germany; New York, NY, USA, 2006. [CrossRef]
27. Karniadakis, G.E.M.; Beskok, A.; Gad-el-Hak, M. Micro flows: Fundamentals and simulation. *Appl. Mech. Rev.* **2002**, *55*, B76. [CrossRef]
28. Hussain, A.; Muneer, Z.; Malik, M.Y.; Ali, S. Formulating the behavior of thermal radiation and magnetic dipole effects on Darcy-Forchheimer grasped ferrofluid flow. *Canad. J. Phys.* **2019**, *97*, 938–949. [CrossRef]

29. Forchheimer, P. Wasserbewegung durch boden. *Z. Ver. Deutsch. Ing.* **1901**, *45*, 1782–1788.
30. Pal, D.; Mondal, H. Hydromagnetic convective diffusion of species in Darcy—Forchheimer porous medium with non-uniform heat source/sink and variable viscosity. *Int. Commun. Heat Mass Transf.* **2012**, *39*, 913–917. [CrossRef]
31. Ganesh, N.V.; Hakeem, A.K.A.; Ganga, B. Darcy–Forchheimer flow of hydromagnetic nanofluid over a stretching/shrinking sheet in a thermally stratified porous medium with second order slip, viscous and Ohmic dissipations effects. *Ain Shams Eng. J.* **2018**, *9*, 939–951. [CrossRef]
32. Seth, G.S.; Mandal, P.K. Hydromagnetic rotating flow of Casson fluid in Darcy-Forchheimer porous medium. *MATEC Web Conf.* **2018**, *192*, 02059. [CrossRef]
33. Seddeek, M.A. Influence of viscous dissipation and thermophoresis on Darcy–Forchheimer mixed convection in a fluid saturated porous media. *J. Colloid Interface Sci.* **2006**, *293*, 137–142. [CrossRef]
34. Hayat, T.; Muhammad, T.; Mezal, S.A.; Liao, S.J. Darcy-forchheimer flow with variable thermal conductivity and Cattaneo–Christov heat flux. *Int. J. Numer. Methods Heat Fluid Flow* **2006**, *26*, 2355–2369. [CrossRef]
35. Rajesh, V.; Sheremet, M.A.; Öztop, H.F. Impact of hybrid nanofluids on MHD flow and heat transfer near a vertical plate with ramped wall temperature. *Case Stud. Therm. Eng.* **2021**, *28*, 101557. [CrossRef]
36. Yaseen, M.; Rawat, S.K.; Shafiq, A.; Kumar, M.; Nonlaopon, K. Analysis of heat transfer of mono and hybrid nanofluid flow between two parallel plates in a Darcy porous medium with thermal radiation and heat generation/absorption. *Symmetry* **2022**, *14*, 1943. [CrossRef]
37. Raza, R.; Naz, R.; Abdelsalam, S.I. Microorganisms swimming through radiative Sutterby nanofluid over stretchable cylinder: Hydrodynamic effect. *Numer. Methods Partial. Differ. Equ.* **2022**, 1–20. [CrossRef]
38. Faizan, M.; Ali, F.; Loganathan, K.; Zaib, A.; Reddy, C.A.; Abdelsalam, S.I. Entropy Analysis of Sutterby Nanofluid Flow over a Riga Sheet with Gyrotactic Microorganisms and Cattaneo–Christov Double Diffusion. *Mathematics* **2022**, *10*, 3157. [CrossRef]
39. Bhattacharyya, K. Effects of radiation and heat source/sink on unsteady MHD boundary layer flow and heat transfer over a shrinking sheet with suction/injection. *Front. Chem. Sci. Eng.* **2011**, *5*, 376–384. [CrossRef]
40. Mukhopadhyay, S. Slip effects on MHD boundary layer flow over an exponentially stretching sheet with suction/blowing and thermal radiation. *Ain Shams Eng. J.* **2013**, *4*, 485–491. [CrossRef]
41. Marin, M.; Öchsner, A. The effect of a dipolar structure on the Hölder stability in Green-Naghdi thermoelasticity. *Contin. Mech. Thermodyn.* **2017**, *29*, 1365–1374. [CrossRef]
42. Marin, M. Cesaro means in thermoelasticity of dipolar bodies. *Acta Mech.* **1997**, *122*, 155–168. [CrossRef]
43. Liao, S. The Proposed Homotopy Analysis Technique for the Solution of Nonlinear Problems. Ph.D. Thesis, Shanghai Jiao Tong University, Shanghai, China, 1992.
44. Liao, S. A kind of approximate solution technique which does not depend upon small parameters. II. An application in fluid mechanics. *Int. J. Nonlinear Mech.* **1997**, *32*, 815–822. [CrossRef]
45. Liao, S. On the analytic solution of magnetohydrodynamic flows of non-Newtonian fluids over a stretching sheet. *J. Fluid Mech.* **2003**, *488*, 189–212. [CrossRef]
46. Liao, S. A new branch of solutions of boundary-layer flows over an impermeable stretched plate. *Int. J. Heat Mass Transf.* **2005**, *48*, 2529–2539. [CrossRef]
47. Liao, S. An optimal homotopy-analysis approach for strongly nonlinear differential equations. *Commun. Nonlinear Sci. Numer. Simul.* **2010**, *15*, 2003–2016. [CrossRef]
48. Liao, S.; Tan, Y. A general approach to obtain series solutions of nonlinear differential equations. *Stud. Appl. Math.* **2007**, *119*, 297–354. [CrossRef]
49. Daniel, Y.S.; Daniel, S.K. Effects of buoyancy and thermal radiation on MHD flow over a stretching porous sheet using homotopy analysis method. *Alex. Eng. J.* **2015**, *54*, 705–712. [CrossRef]
50. Chamkha, A.J. Thermal radiation and buoyancy effects on hydromagnetic flow over an accelerating permeable surface with heat source or sink. *Int. J. Eng. Sci.* **2000**, *38*, 1699–1712. [CrossRef]